JACS
JOURNAL OF THE AMERICAN CHEMICAL SOCIETY
pubs.acs.org/JACS
Article

A′-Site Dipole Magnitude and Direction Dominate the Ionization Energy and Electron Affinity of Layered Metal-Halide Perovskites

Harindi R Atapattu, Sahar Bayat, Henry Pruett, Anton S Perera, Tareq Hossain, Keerthan R. Rao, Kevin Pedersen, Augustine Yusuf, Sean Parkin, Chad Risko, and Kenneth R. Graham*

Cite This: J. Am. Chem. Soc. 2025, 147, 26898−26906
Read Online
ACCESS | Metrics & More | Article Recommendations | Supporting Information

ABSTRACT: Layered metal halide perovskites (LHPs), often referred to as 2D HPs, are promising materials for developing optoelectronics due to their tunable optoelectronic properties and improved stability compared to nonlayered (3D) metal halide perovskites. For integration into electronic devices, it is critical to appropriately adjust the work function (WF) and transport energies of the LHPs to promote efficient charge transfer between materials in the device stack. The transport energies of LHPs can be modified by changing the A′-site cation structure, inorganic sheet thickness, and the metal cation or halide anion. Here, we investigate how the A′-site cation structure influences the WF, ionization energy (IE), and electron affinity (EA) of n = 1 Sn- and Pb-based LHPs with a series of *ortho*- and *para*-functionalized phenethylammonium (PEA) iodide derivatives. To accurately assign the IE and EA, we develop a fitting method where the instrumental broadening, σ_{IB}, in ultraviolet and low-energy inverse photoemission spectroscopy (UPS and LEIPS, respectively) is accounted for. Density functional theory calculations combined with UPS and LEIPS measurements show that the dipole magnitude and direction of the A′-site cation exert a dominant influence on the WF, IE, and EA. Here, the direction and magnitude of the dipole, as manipulated through the strength and position of the electron-withdrawing or -donating substituent on PEA, can tune the WF by up to 1.2 eV, the IE by up to 0.9 eV, and the EA by up to 1.2 eV. The crystal structures indicate that the Sn−I−Sn bond angles have a clear influence over the optical gap; however, the influence of these Sn−I−Sn bond angles on the transport energies is dwarfed by the effect of the A′ dipole. These results provide insight into how to tune the WF and transport energies of LHPs for optoelectronic device integration.

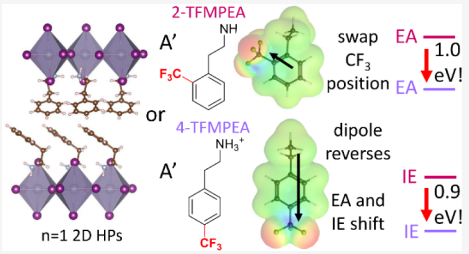

INTRODUCTION

Metal halide perovskites (HPs) are attractive materials for a variety of optoelectronic devices.[1−6] They exhibit desirable optoelectronic properties, such as high absorption coefficients, good defect tolerance, and tunable band gaps.[7,8] While the majority of HP research has been on nonlayered (three-dimensional, 3D) HPs, layered HPs (LHPs) provide several advantages. Layered HPs, often referred to as 2D HPs, are a category of HPs where the inorganic structure is divided into discrete layers by incorporating large organic A′-site cations.[9−11] The interest in LHPs arises in part from their desirable and tunable optoelectronic properties, which include high exciton binding energies relative to 3D HPs,[12] enhanced stability compared to 3D HPs,[13] high photoluminescence quantum yields,[14] and widely tunable light-emission wavelengths.[9] Thus, LHPs are being investigated for use in light-emitting diodes (LEDs), transistors, photovoltaics, and photodetectors.[15−22]

Layered HPs have a general formula of $A'_mA_{n-1}B_nX_{3n+1}$, where A′, A, B, and X represent the large organic cation that cannot fit within the 3D HP structure, monovalent small cation that can incorporate into the 3D HP structure, divalent metal cation, and halide anion, respectively.[9,10] In these LHPs it is often observed that a Ruddlesden−Popper (RP) phase results when m = 2 and a Dion-Jacobson (DJ) phase when m = 1.[9,10] The thickness of the metal halide sheets, in terms of the number of inorganic octahedra between the layers of A′ cations, is indicated by n.[9,10]

Appropriate transport energies and interfacial energetics in LHP or HP containing devices are important for ensuring that charge carriers are efficiently transferred to neighboring materials in a device stack and for modeling device physics in optoelectronic devices.[2,23−25] The LHP transport energies can be tuned by changing the structure of the A′ cation, changing the metal halide sheet thickness (i.e., n in $A'_mA_{n-1}B_nX_{3n+1}$), and varying the metal and halide ions.[26,27] While there are only a few options for B and X, the number of different A′ cations that can be used is nearly limitless. Here, the A′ cation structure will influence the B-X-B bond angle, B-

Received: May 21, 2025
Revised: July 8, 2025
Accepted: July 9, 2025
Published: July 16, 2025

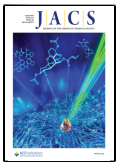

https://doi.org/10.1021/jacs.5c08621
J. Am. Chem. Soc. 2025, 147, 26898−26906

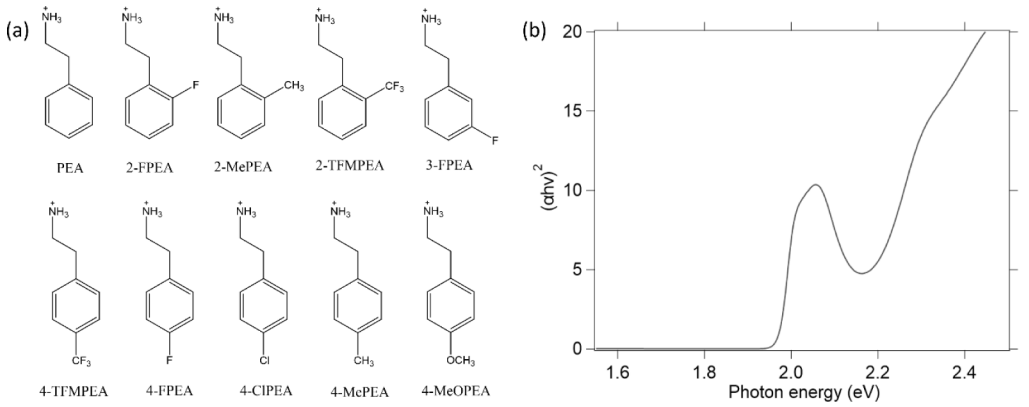

Figure 1. (a) Chemical structures of A'-site cations and (b) Tauc plot for an n = 1 PEA_2SnI_4 film.

X bond length, and interlayer distance.[9,28−30] For example, when the A'-site cation is changed from butylammonium (BA) to phenethylammonium (PEA) in A'_2PbI_4, the Pb−I−Pb bond angle changes from 147.6 to 153.0°.[31,32] To further tune the interactions between the organic and inorganic layers, A' cations with functional groups can be used.[9,27] For example, ammonium cations with alcohol groups,[33] halogen groups,[34] and carboxylic acid[35] groups have all been employed to alter the LHP's structural and optical properties.

While many LHPs have been synthesized and their crystal structures and optical properties investigated, there have been limited efforts to understand how the A' cation structure impacts the work function (WF), ionization energy (IE), and electron affinity (EA) of these materials. Here, the Kahn group showed that Pb−I−Pb bond angle distortion and octahedral tilting in the crystal structure influences the energy levels of n = 1 LHPs.[36,37] These distortions lead to IE and EA variations of up to 0.52 eV as the bond angle varies from 143 to 174°. The change in the metal halide sheet thickness, n, will also influence the IE and EA of LHPs. For example, as n increases from 1 to 5 in $BA_2MA_{n-1}Pb_nI_{3n+1}$, the bandgap decreases from 2.8 to 1.6 eV.[38]

Ultraviolet and inverse photoemission spectroscopy (UPS and IPES, respectively) are typically used to experimentally determine the WF, IE, and EA of 3D and LHPs, although determining the IE and EA for HPs is not trivial. For example, several different approaches for extracting the IE and EA from experimentally measured spectra are used for 3D HPs. Approaches such as linear extrapolation to the band edge,[39] Gaussian fitting,[40] and density functional theory (DFT) guided fitting of experimental spectra[7] are all used to assign the IE and EA in 3D HPs. In 2D HPs, DFT calculations show the presence of a higher density of states (DOS) near the band edges as compared to 3D HPs, which led several groups to assign the IE and EA of LHPs using a linear extrapolation method.[37,41,42] The use of the linear extrapolation method to assign the energy levels of LHPs can also be difficult, as the fitting region can be subjective and the IE or EA can change based on the noise floor of the instrument.

Knowledge of the transport energies of LHPs are critical for enabling effective device integration and guiding the design of new materials; thereby, it is desirable to have a robust procedure for extraction of the IE and EA from experimental UPS and low-energy inverse photoemission spectroscopy (LEIPS) spectra. In addition, establishing how A' cation structure influences the WF, IE, and EA requires investigation of LHPs with structurally similar A' cations. In this work we investigate the influence of a series of phenethylammonium (PEA) iodide derivatives on the WF, IE, and EA of tin-based LHPs. Here, we change the nature of the PEA derivatives by adding electron withdrawing and electron donating functional groups at the *ortho* and *para* positions of the phenyl ring, determine the crystal structures of the LHPs, and determine the WF, IE and EA using UPS and LEIPS. To accurately assign IE and EA values we propose a fitting method that accounts for the instrumental broadening of the UPS and LEIPS instruments. We find that the dipole direction of the A' cation strongly impacts the WF, IE, and EA of the LHPs.

RESULTS AND DISCUSSION

The series of PEA derivatives used herein as A'-site cations in A'_2SnI_4 are depicted in Figure 1. These A' cations were used to make layered tin-based HP thin films of n = 1 and the films were characterized by ultraviolet−visible (UV−vis) absorbance spectroscopy, Figure S1, and X-ray diffraction (XRD), Figure S2. The formation of the n = 1 thin films is evident from the UV−vis and XRD spectra, with XRD spectra showing strong peaks from the (002) planes for all the LHPs. First, to extract the optical gaps we used Tauc plots,[29] as shown for PEA_2SnI_4 in Figures 1b and S1 for the other LHPs. The Tauc plots were modeled using the equation $(\alpha h\nu)^2 = B(h\nu - E_g)$,[29] where α is the absorption coefficient, $h\nu$ is the photon energy, E_g is the band gap, and B is a constant. The optical gaps for the LHPs were extracted from the Tauc plots and an optical gap of 1.97 eV was determined for PEA_2SnI_4, which agrees with a previous report.[43]

UPS and LEIPS measurements were carried out on thin films of PEA_2SnI_4 to determine the bandgap, WF, IE, and EA. These LHPs suffer from sample charging and sample damage during LEIPS measurements if the films are too thick (e.g., >25 nm), which we attribute to poor out-of-plane charge transport. Thin films (≤15 nm) were thus investigated to eliminate or minimize sample charging. Initially, we used two different methods to assign the IE and EA, including the linear extrapolation method reported by Silver et al.[41] for LHPs and the Gaussian fitting method reported by Endres et al.[40] for 3D HPs. For PEA_2SnI_4, an IE and EA of 4.97 ± 0.05 and 3.33 ± 0.10 eV are extracted with the linear extrapolation method, while Gaussian fitting results in an IE and EA of 4.81 ± 0.05 and 3.53 ± 0.10 eV, as shown in Figure S3. The bandgap derived from linear and Gaussian fitting is 1.64 and 1.28 ± 0.11 eV, respectively, which are unrealistic given the 1.97 eV optical

https://doi.org/10.1021/jacs.5c08621
J. Am. Chem. Soc. 2025, 147, 26898−26906

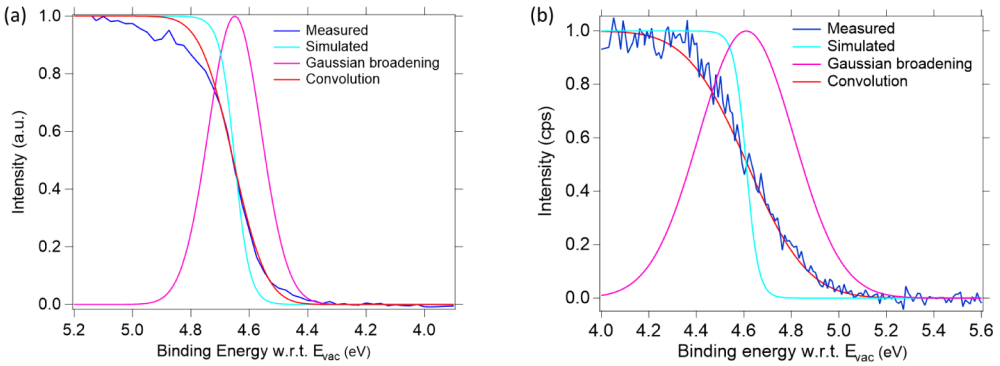

Figure 2. Measured and simulated (Fermi distribution at T = 295 K) UPS (a) and LEIPS (b) spectra for sputter-cleaned Ag, the extracted instrumental broadening component, and the convolution of the simulated spectra with instrumental broadening.

gap. Therefore, to assign the IE and EA we developed and deployed a new fitting method where instrumental broadening is quantified and removed to determine the IE and EA. Notably, Yoshida also subtracted instrumental broadening in the initial report and subsequent applications of LEIPS,[44,45] albeit using a different approach than that reported here. In Yoshida's work a constant instrumental broadening value, as determined from fitting the full width half-maximum of the Fermi edge of silver, was subtracted from the measured LUMO onset as determined by a linear fitting process. In contrast to molecular organic semiconductors that often yield unambiguous HOMO and LUMO onsets, HPs typically show more broad onsets to the valence and conduction bands that are more reproducibly extracted using a Gaussian fitting procedure.[40] The method we report here increases the robustness and versatility of accounting for instrumental broadening, and is applicable to materials with both high and low densities of states near the band edges.

To determine the instrumental broadening, a thermally evaporated 100 nm thick Ag film was deposited and sputter cleaned in an ultrahigh vacuum system with an Ar^+ ion gun. UPS and LEIPS measurements were collected from the sputter-cleaned Ag sample and the spectra are shown as "measured" in Figure 2a,b. The simulated Fermi edge of the metal is calculated using the Fermi function at T = 295 K, which is represented as the simulated spectra in Figure 2a,b. To determine the instrumental broadening in our UPS and LEIPS measurements, the simulated Fermi function was convolved with a Gaussian representing instrumental broadening. The instrumental broadening Gaussian width was adjusted such that the convolution obtained matched the measured UPS and LEIPS of the Ag sample at the Fermi edge. With this process, we determine the width of the Gaussian from instrumental broadening, σ_{IB}, to be 0.09 and 0.20 eV for UPS and LEIPS, respectively.

With the instrumental broadening contributions defined, Figure 3 shows the corrected (i.e., instrumental broadening removed) spectra and extracted IE and EA. In this IE and EA extraction procedure, the experimentally measured onset regions for the UPS and LEIPS spectra are first fit with Gaussians, as shown by solid lines. The measured standard deviation, σ_M, is determined from the Gaussian fit to the onset region of the measured spectra. With σ_{IB} and σ_M known, we next use a fitting routine with the convolution function (Python code given in the SI) to determine the corrected Gaussian fit to the material's DOS onset with instrumental broadening removed. This corrected Gaussian fit, with a

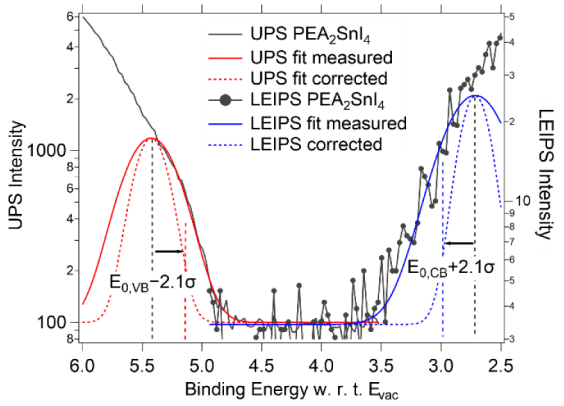

Figure 3. Extraction of IE and EA for PEA_2SnI_4 from the UPS and LEIPS spectra. The solid red and blue lines indicate the measured Gaussian fits, and the dashed lines indicate the corrected Gaussian fits.

standard deviation of σ_C, is shown by the dashed lines in Figure 3. Briefly, the fitting routine relies on the use of the convolve function to convolve the instrumental broadening Gaussian with the corrected Gaussian to match the measured Gaussian fit. With σ_{IB} and σ_M known, σ_C is manually guessed until the convoluted Gaussian matches the measured Gaussian. The value for σ_C is taken when the σ_M value from the Python code matches with the σ_M value from the Gaussian fit to the measured spectra. The IE and EA are then calculated by subtracting or adding, respectively, $2.1\sigma_C$ to or from the Gaussian peak position. This $2.1\sigma_C$ is based on the intersection of the tangent to a Gaussian at half-maximum with the background, as shown in Figure S4, and yields the same value as a linear fit.

Applying the fitting routine to remove instrumental broadening we determine the IE of PEA_2SnI_4 to be 5.15 ± 0.05 eV and the EA to be 2.98 ± 0.10 eV for PEA_2SnI_4. This extraction method results in a bandgap for PEA_2SnI_4 of 2.17 ± 0.11 eV, which is 0.20 eV larger than the optical gap of 1.97 eV. The exciton binding energy (E_b) determined based on our UPS and LEIPS measured bandgap and the optical gap is therefore 0.20 ± 0.11 eV. This value is in good agreement with the E_b of 0.128 ± 0.016 eV for PEA_2SnI_4 reported based on electroabsorption measurements and the E_b of 0.19 eV for PEA_2SnI_4 extracted from temperature-dependent photoluminescence.[12,46,47] This agreement supports that our fitting method enables extraction of an accurate bandgap for LHPs from UPS and LEIPS measurements.

https://doi.org/10.1021/jacs.5c08621
J. Am. Chem. Soc. 2025, 147, 26898−26906

We next determine how the A' structure impacts the WF, IE, EA, and bandgap. The crystal structure, and particularly the Sn−I−Sn bond angles, are known to impact the optical gap and bandgap of LHPs. The crystal structures are shown in Figures 4 and S5 for the tin LHPs investigated here. The single

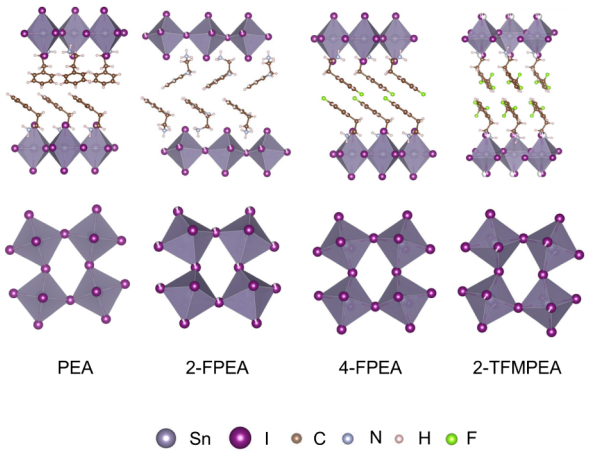

Figure 4. Crystal structures for A'_2SnI_4. The top row is viewed parallel to the plane of the layers, while the bottom presents a view that is perpendicular to the inorganic sheets. The A' cations were removed from the structures in the bottom row to more adequately show the Sn−I−Sn bond angles.

crystals were made using the ethanol-assisted method reported by Ding et al.[48] Unfortunately, we were unable to obtain crystal structures for 4-TFMPEA and 4-MePEA. The six LHPs with known crystal structures show that all cations indeed make RP-phase n = 1 LHPs. The Sn−I−Sn bond angle varies from 148.5 to 155.9° depending on the A' cation. The lowest angle is observed for 2-TFMPEA and the highest for PEA. The *ortho*-substituted PEA derivatives show decreased Sn−I−Sn bond angles compared to PEA and 4-FPEA, indicating more distorted crystal structures. Corresponding with the smallest Sn−I−Sn bond angle, 2-TFMPEA displays the largest optical gap of 2.16 eV. This optical gap generally decreases as the Sn−I−Sn bond angle increases. For example, PEA and 4-FPEA show the largest Sn−I−Sn bond angles of 155.9 and 155.5° and the smallest optical gaps of 1.97 and 1.95 eV, respectively. On the other hand, the UPS-LEIPS measured bandgap does not appear to correlate strongly with the Sn−I−Sn bond angles. The bandgaps extracted from UPS-LEIPS measurements are often 0.1 to 0.3 eV greater than the optical gap, which is consistent with the range of exciton binding energies previously reported for PEA_2SnI_4;[12,46,47] however, a few of the LHPs have bandgaps that result in exciton binding energies that are outside of this expected range. More detailed investigation using more precise methods of determining the E_b are currently being pursued.

To understand how the structure of the A'-site cation impacts the WF, IE, and EA we must consider the molecular dipoles, as the magnitude, direction, and orientation of dipolar or quadrupolar moments of both self-assembled monolayers (SAMs) and organic semiconductors can have a large impact on these properties.[49−53] Specifically, the component of the molecular dipole (or quadrupole) perpendicular to the substrate can significantly impact these values, which does mean that the WF, IE, and EA are likely to vary with the orientation distribution of the LHPs present in the specific sample investigated. To understand how the dipole moments of the A' cations impact the WF, IE, and EA, we first determined the net dipole moments of the A' cations in their neutral form using density functional theory (DFT) at the ωB97XD/LANL2DZ level of theory. When evaluating the dipole moments, we used the conformation of the A'-site molecule extracted from the LHP crystal structure when the crystal structure was available. For crystal structures that were not available, we considered two orientations of ethylamine. In one orientation the ethylamine is in plane with the benzene ring (in the xz plane), and in the other the ethylamine is out of plane with respect to the benzene ring (in the yz plane), as shown in Figure 5. The out-of-plane conformation is the most stable, by 0.3 to 3.1 kcal/mol depending on the A' molecule. Consistent with the higher stability, the out-of-plane conformation is more similar to the conformation found in the LHPs when the crystal structures are known, as evident from the crystal structures presented in Figures 4 and S5. The total dipole moments for either the crystal structure determined conformation or the out-of-plane conformation are shown in Table 1. For comparison the dipole moment for both in-plane and out-of-plane conformations for all A'-site molecules are shown in Tables S2 and S3.

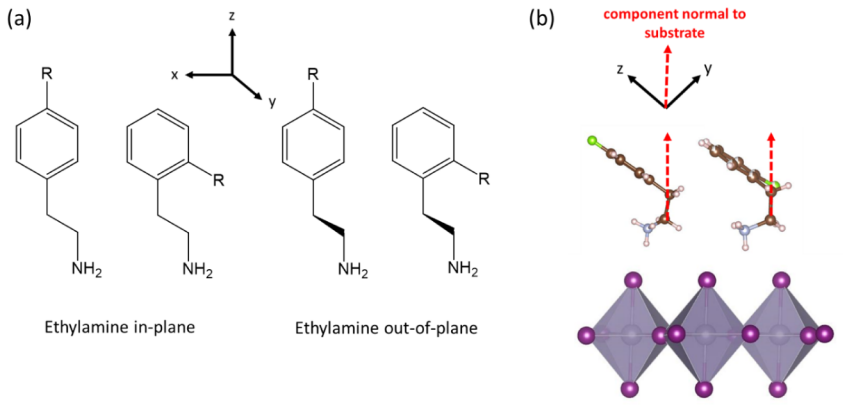

Figure 5. (a) Depiction of the in-plane and out-of-plane conformations used for DFT calculations when the crystal structure is not known. The axes are defined such that the z axis points in the direction of the alkyl C to phenyl C (CH_2−C) bond and the y axis is perpendicular to the plane of the phenyl ring. (b) Crystal structure views of 4-FPEA (left) and 2-FPEA (right) showing that the dipole components in the z and y directions have the most significant components perpendicular to the inorganic sheets, and thereby perpendicular to the substrate.

https://doi.org/10.1021/jacs.5c08621
J. Am. Chem. Soc. 2025, 147, 26898−26906

Table 1. Work Function (WF), Ionization Energy (IE), Electron Affinity (EA), Bandgap, Dipole Components, Optical Gap, and Sn−I−Sn Bond Angle for the LHP Thin Films

A' in A'_2SnI_4	WF (eV)	IE (eV)	EA (eV)	Bandgap (eV)	D_y of A' (D)	D_z of A' (D)	D_N of A' (D)	Optical gap (eV)	Sn−I−Sn bond angle (°)
PEA	4.67	5.15	2.98	2.17	1.08[a]	−0.28[a]	0.73	1.97	155.9
2-FPEA	4.35	5.01	3.08	1.93	0.72[a]	1.29[a]	1.29	2.02	151.2
2-TFMPEA	4.60	5.07	2.78	2.29	1.01[a]	1.29[a]	1.61	2.16	148.5
2-MePEA	4.52	5.27	3.07	2.20	1.17[a]	−0.45[a]	0.20	2.14	151
3-FPEA	4.9	5.46			0.81[a]	−1.02[a]	0.05	1.99	153.7
4-MeOPEA	4.42	4.92	2.55	2.37	0.91[a]	0.61[a]	1.09	1.98	154.0
4-FPEA	5.17	5.56	3.24	2.32	1.07[a]	−2.16[a]	−0.35	1.95	155.5
4-MePEA	4.55	5.09	2.58	2.51	1.06[b]	0.17[b]	0.75	1.94	-
4-TFMPEA	5.55	5.95	3.74	2.21	1.27[b]	−4.76[b]	−1.70	1.96	-
4-ClPEA	5.25	5.68			1.05[c]	−2.41[c]	−0.52	1.94	-

[a]Based on the conformation extracted from the crystal structure. [b]Based on the out-of-plane conformation. [c]Based on substituting Cl for F in the conformation extracted from the crystal structure of 4-FPEA.

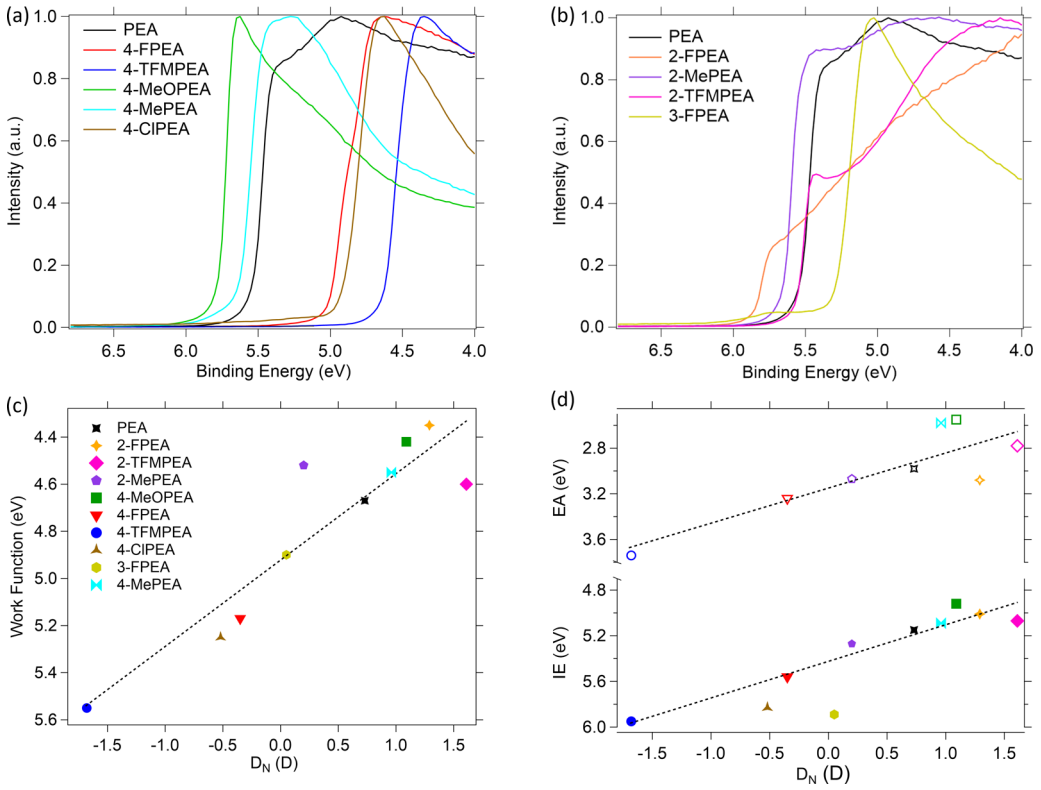

Figure 6. Secondary electron cutoff (SECO) regions of the Sn LHPs UPS spectra for the (a) *para*-substituted derivatives and (b) *ortho*-substituted derivatives. Plots of (c) WF vs D_N and (d) EA and IE vs D_N for the Sn LHP films. The WF is determined by the formula WF = $h\nu$ − SECO, where $h\nu$ is 10.2 eV for these UPS measurements. In (d) the filled markers are IE points and open markers are EA points.

From GISAXS and GIWAXS measurements, it is apparent that the dominant orientation of the 2D sheets is with the 2D planes oriented parallel with the substrate surface.[54,55] Thus, the major influence on the IE, WF, and EA should be the component of the dipole that is oriented perpendicular to the plane of the inorganic sheets. Figure 5b shows that the y- and z-components of the dipole have significant contributions in the direction perpendicular to the inorganic sheets, while the x-component is generally aligned parallel to the inorganic sheet. Across this family of PEA derivatives, the z-component of the dipole moment (D_z) varies from −4.76 D for 4-TFMPEA to +1.29 D for 2-TFMPEA, with the variations depending on both the strength and position of the electron withdrawing or donating substituent. When the electron withdrawing strength of the substituent in the *para* position increases, D_z becomes increasingly more negative. For example, in going from PEA to 4-FPEA to 4-TFMPEA D_z changes from −0.28 to −2.16 to −4.76 D, respectively. By contrast, when PEA is substituted at the *ortho* position D_z becomes increasingly more positive as the eletron withdrawing strength of the substituent increases. For example, D_z is −0.45 D for 2-MePEA and 1.29 D for 2-TFMPEA due to the stronger electron withdrawing CF_3 group.

The WF of the tin LHPs should vary in accordance with the sign and magnitude of the z- and y-components of the dipole moments of the A' cation. This expectation is based on the inorganic sheets being primarily oriented with the SnI_2 planes parallel to the substrate surface and the films being terminated with the A' cations, as is expected based on previous literature and grazing incidence X-ray scattering measurements.[54,55] The measured WFs from the UPS spectra are shown in Table 1,

https://doi.org/10.1021/jacs.5c08621
J. Am. Chem. Soc. 2025, 147, 26898−26906

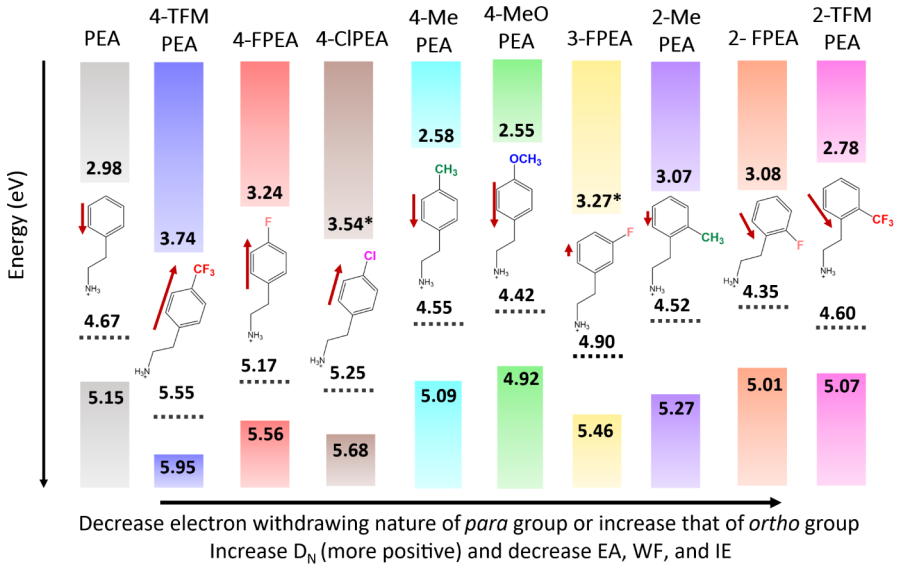

Figure 7. EA (top), WF (middle dashed lines), and IE (bottom) for the series of A'$_2$SnI$_4$ investigated along with the relative dipole moments indicated by the length of the red arrows. *The EAs for 4-ClPEA$_2$SnI$_4$ and 3-FPEA$_2$SnI$_4$ were calculated by adding the optical gap to the IE values.

with the secondary electron cutoff (SECO) region of the UPS spectra shown in Figure 6a,b. For *para*-substituted derivatives, the WF significantly increases when increasing the electron withdrawing nature of the substituent. For example, with the most electron donating methoxy group the work function is 4.42 eV, while the most electron withdrawing CF_3 group leads to a work function of 5.55 eV. A similarly large variation in WF can be obtained by changing the position of the substituent on PEA. For example, by changing the position of a single fluorine atom from the *para* to *ortho* position the WF decreases by over 0.8 eV, from 5.17 to 4.35 eV. These are massive variations in the WF and they result from changing only a single substituent or its position on PEA.

The plot of the WF vs the A' dipole component that is normal to the SnI_2 plane (D_N) is displayed in Figure 6c. Here, D_N was calculated by determining the angle(s) between the phenyl group and the SnI_2 plane based on the crystal structure and the sum of the D_z and D_y components in the direction normal to the SnI_2 plane (see Figure S6). All *para* substituted derivatives have angles between 34 and 36°, thereby an angle of 35° was used for the *para* substitued derivatives with unknown crystal structure. Figure 6c shows that the WF indeed varies with D_N. For example, as D_N decreases from 1.29 to −0.35 to −1.70 D for 2-FPEA, 4-FPEA, and 4-TFMPEA the WF increases from 4.35 to 5.17 to 5.55 eV, respectively.

In addition to the WF, the UPS and LEIPS spectra shown in Figure S7 through S10 and summarized in Figure 6d highlight that the nature and position of the substituent has a large influence on the IE and EA of the LHPs. These shifts parallel that of the WF and resemble trends seen in organic semiconductors, where the direction of the quadrupole moment of the organic semiconductor relative to the substrate results in shifts in the IE.[51−53] Figure 6d shows the relationship between D_N and the IE and EA for the series of Sn LHPs, where the IE and EA for the LHPs were determined using the described method to remove instrumental broadening. As can be seen in Figure 6d, as D_N increases from −1.7 to +1.6 the IE and EA both decrease by ca. 1 eV.

The relationships between the electron withdrawing group strength and position, D_N, WF, IE, and EA are highlighted in Figure 7 and SI Figures S8 and S9. In general, Figure 7 shows that the WF of all the Sn LHPs is closer to the IE than the EA, which is commonly observed for Sn HPs due to defects that lead to *p*-type character.[7,56,57] For the *para* substituted derivatives, as the strength of the electron withdrawing group increases and D_z decreases from −0.28 to −2.16 to −4.76 D for PEA, 4-FPEA, and 4-TFMPEA, the IE increases from 5.15 to 5.56 to 5.95 eV, respectively. Similar increases in the EA from 2.98 to 3.24 to 3.74 eV, respectively, are also observed for this series. Alternatively, as the electron donating strength of the substituents at the *para* position increase and D_N increases, the IE and EA decrease. For example, 4-MeOPEA results in a decreased EA, WF, and IE relative to 4-MePEA and PEA.

Figures 7 and S9 illustrate how switching a substituent from the *para* to the *ortho* position of the A' cation impacts the UPS and LEIPS spectra for the LHP films. For fluorine, Figure S9a, when the position is changed from *ortho* to *para* D_z decreases from 1.29 to −2.16 D, which results in an increase of the IE from 5.01 to 5.56 eV and increase in the EA from 3.07 to 3.24 eV. Similar trends are reproduced for 2-TFMPEA and 4-TFMPEA, Figure S9b, where the dipole in the *z*-direction decreases from 1.29 to −4.76 D and the IE and EA increase by 0.88 and 0.96 eV, respectively. These trends are reversed for the electron donating methyl groups. Here, D_z increases from −0.45 to 0.17 D in going from 2-MePEA to 4-MePEA, which results in a decrease in the IE and EA of 0.18 and 0.49 eV, respectively.

Based on the data presented, the change in IE, EA, and WF for this series of Sn LHPs is dominated by the A'-site dipole with minimal influence from changes in the crystal structure. For example, going from 2-TFMPEA to 4-TFMPEA may be proposed to relate to the changes in crystal structure, as 2-TFMPEA shows the highest distortion with the smallest Sn−I−Sn bond angle. However, a similar change is observed in going from 2-FPEA to 4-FPEA, where 2-FPEA is much less distorted than 2-TFMPEA. Furthermore, in going from 2-MePEA to 4-MePEA the opposite change in IE and EA is observed, which solidifies the role of the dipole. This comparison highlights that the dipole of the A'-site molecule exerts a dominant influence on the IE and EA, and that shifting

https://doi.org/10.1021/jacs.5c08621
J. Am. Chem. Soc. 2025, 147, 26898−26906

the position of a substituent can change the IE and EA by nearly 1 eV.

To test the generality of these trends we performed UPS measurements on a similar series of A'_2PbI_4 analogues, with these UPS plots and fits shown in Figure S12. Similar to the trend with 3D HPs, the Pb-based LHPs show increased IEs relative to their Sn counterparts.[7] The WF and IE values were extracted using the previously detailed methods and these values are plotted vs D_N in SI Figure S13. The same trends as observed for the Sn LHP series are also apparent for the Pb series, with the WF and IE decreasing as D_N increases from negative to positive. This Pb LHP series shows even greater changes in WF and IE with the change of the dipole moment of the A'-site cation, with variations of ca. 1.5 eV in both WF and IE as the A'-site cation is varied.

CONCLUSION

Our results show that changing the electron withdrawing strength or position of substituents on A' cations in LHPs directly impacts the A' dipole moment and causes a significant shift in the WF, IE, and EA of LHPs. Varying the A' dipole strength enables the WF of LHPs to be adjusted by up to 1.2 eV, with comparable changes in the IE and EA. Overall, our study emphasizes that the A' cation structure plays a critical role in tuning electronic properties in layered Sn HPs. Furthermore, we present a new fitting method to account for instrumental broadening in UPS and LEIPS measurements. Applying this fitting method provides accurate IE and EA values for LHPs and should be widely applicable to other material classes. We expect this fitting method will be especially useful to researchers performing and interpreting UPS, IPES, and LEIPS measurements.

In terms of adjusting the WF, IE, and EA in LHPs, the A' dipole is the most influential parameter. Additional parameters, such as the orientation distribution of inorganic sheets, are also likely to have a major effect on these parameters. Investigating parameters such as this orientation distribution and changes in Sn−I−Sn bond angles in the absence of significant changes in the A' dipole will also be important for directing the design and selection of LHPs. In general, the insights gained through this work will enable more efficient selection and design of LHPs, or their neighboring transport layers, for application in optoelectronic devices.

ASSOCIATED CONTENT

Supporting Information

The Supporting Information is available free of charge at https://pubs.acs.org/doi/10.1021/jacs.5c08621.

Synthesis procedures for PEAI derivatives and single crystals; characterization procedures; computational methods; a detailed explanation of instrumental broadening correction along with the Python code; UV−vis absorbance spectra, XRD spectra, and UPS and LEIPS data for Sn LHP thin films; UPS data for Pb LHP thin films; crystal structure data for A'_2SnI_4; schematic of D_N determination; crystal structure views; and DFT calculated molecular dipole components (PDF)

Accession Codes

Deposition Numbers 2400812 and 2452782 contain the supplementary crystallographic data for this paper. These data can be obtained free of charge via the joint Cambridge Crystallographic Data Centre (CCDC) and Fachinformationszentrum Karlsruhe Access Structures service.

AUTHOR INFORMATION

Corresponding Author

Kenneth R. Graham − *Department of Chemistry, University of Kentucky, Lexington, Kentucky 40506, United States;* orcid.org/0000-0002-6387-3998; Email: kenneth.graham@uky.edu

Authors

Harindi R Atapattu − *Department of Chemistry, University of Kentucky, Lexington, Kentucky 40506, United States*

Sahar Bayat − *Department of Chemistry, University of Kentucky, Lexington, Kentucky 40506, United States*

Henry Pruett − *Department of Chemistry, University of Kentucky, Lexington, Kentucky 40506, United States*

Anton S Perera − *Department of Chemistry, University of Kentucky, Lexington, Kentucky 40506, United States*

Tareq Hossain − *Department of Chemistry, University of Kentucky, Lexington, Kentucky 40506, United States;* orcid.org/0000-0001-5559-1168

Keerthan R. Rao − *Department of Chemistry, University of Kentucky, Lexington, Kentucky 40506, United States*

Kevin Pedersen − *Department of Chemistry, University of Kentucky, Lexington, Kentucky 40506, United States*

Augustine Yusuf − *Department of Chemistry, University of Kentucky, Lexington, Kentucky 40506, United States*

Sean Parkin − *Department of Chemistry, University of Kentucky, Lexington, Kentucky 40506, United States*

Chad Risko − *Department of Chemistry, University of Kentucky, Lexington, Kentucky 40506, United States;* orcid.org/0000-0001-9838-5233

Complete contact information is available at: https://pubs.acs.org/10.1021/jacs.5c08621

Notes

The authors declare no competing financial interest.

ACKNOWLEDGMENTS

H.R.A., H.P., T.H., K.P., and K.R.G acknowledge funding from the National Science Foundation through DMR-2102257. A.Y. and K.R.G. acknowledge funding from the National Science Foundation through DMR-2349830. S.B., A.S.P., K.R.R., and C.R. acknowledge funding from the National Science Foundation through Cooperative Agreement Number 1849213. Supercomputing resources on the Lipscomb High Performance Computing Cluster were provided by the University of Kentucky Information Technology Department and Center for Computational Sciences (CCS).

REFERENCES

(1) Ma, K.; Atapattu, H. R.; Zhao, Q.; Gao, Y.; Finkenauer, B. P.; Wang, K.; Chen, K.; Park, S. M.; Coffey, A. H.; Zhu, C.; Huang, L.; Graham, K. R.; Mei, J.; Dou, L. Multifunctional Conjugated Ligand Engineering for Stable and Efficient Perovskite Solar Cells. *Adv. Mater.* **2021**, *33* (32), 2100791.

(2) Park, S. M.; Abtahi, A.; Boehm, A. M.; Graham, K. R. Surface Ligands for Methylammonium Lead Iodide Films: Surface Coverage, Energetics, and Photovoltaic Performance. *ACS Energy Lett.* **2020**, *5* (3), 799−806.

(3) Park, S. M.; Wei, M.; Xu, J.; Atapattu, H. R.; Eickemeyer, F. T.; Darabi, K.; Grater, L.; Yang, Y.; Liu, C.; Teale, S.; Chen, B.; Chen, H.; Wang, T.; Zeng, L.; Maxwell, A.; Wang, Z.; Rao, K. R.; Cai, Z.;

Zakeeruddin, S. M.; Pham, J. T.; Risko, C. M.; Amassian, A.; Kanatzidis, M. G.; Graham, K. R.; Grätzel, M.; Sargent, E. H. Engineering ligand reactivity enables high-temperature operation of stable perovskite solar cells. *Science* **2023**, *381* (6654), 209−215.
(4) Wang, K.; Lin, Z.-Y.; Zhang, Z.; Jin, L.; Ma, K.; Coffey, A. H.; Atapattu, H. R.; Gao, Y.; Park, J. Y.; Wei, Z.; Finkenauer, B. P.; Zhu, C.; Meng, X.; Chowdhury, S. N.; Chen, Z.; Terlier, T.; Do, T.-H.; Yao, Y.; Graham, K. R.; Boltasseva, A.; Guo, T.-F.; Huang, L.; Gao, H.; Savoie, B. M.; Dou, L. Suppressing phase disproportionation in quasi-2D perovskite light-emitting diodes. *Nat. Commun.* **2023**, *14* (1), 397.
(5) Liu, X.-K.; Xu, W.; Bai, S.; Jin, Y.; Wang, J.; Friend, R. H.; Gao, F. Metal halide perovskites for light-emitting diodes. *Nat. Mater.* **2021**, *20* (1), 10−21.
(6) Choi, J.; Han, J. S.; Hong, K.; Kim, S. Y.; Jang, H. W. Organic−Inorganic Hybrid Halide Perovskites for Memories, Transistors, and Artificial Synapses. *Adv. Mater.* **2018**, *30* (42), 1704002.
(7) Tao, S.; Schmidt, I.; Brocks, G.; Jiang, J.; Tranca, I.; Meerholz, K.; Olthof, S. Absolute energy level positions in tin- and lead-based halide perovskites. *Nat. Commun.* **2019**, *10* (1), 2560.
(8) Jena, A. K.; Kulkarni, A.; Miyasaka, T. Halide Perovskite Photovoltaics: Background, Status, and Future Prospects. *Chem. Rev.* **2019**, *119* (5), 3036−3103.
(9) Li, X.; Hoffman, J. M.; Kanatzidis, M. G. The 2D Halide Perovskite Rulebook: How the Spacer Influences Everything from the Structure to Optoelectronic Device Efficiency. *Chem. Rev.* **2021**, *121* (4), 2230−2291.
(10) Mao, L.; Stoumpos, C. C.; Kanatzidis, M. G. Two-Dimensional Hybrid Halide Perovskites: Principles and Promises. *J. Am. Chem. Soc.* **2019**, *141* (3), 1171−1190.
(11) Blancon, J.-C.; Even, J.; Stoumpos, C. C.; Kanatzidis, M. G.; Mohite, A. D. Semiconductor physics of organic−inorganic 2D halide perovskites. *Nat. Nanotechnol.* **2020**, *15* (12), 969−985.
(12) Hansen, K. R.; Wong, C. Y.; McClure, C. E.; Romrell, B.; Flannery, L.; Powell, D.; Garden, K.; Berzansky, A.; Eggleston, M.; King, D. J.; Shirley, C. M.; Beard, M. C.; Nie, W.; Schleife, A.; Colton, J. S.; Whittaker-Brooks, L. Mechanistic origins of excitonic properties in 2D perovskites: Implications for exciton engineering. *Matter* **2023**, *6* (10), 3463−3482.
(13) Liao, Y.; Liu, H.; Zhou, W.; Yang, D.; Shang, Y.; Shi, Z.; Li, B.; Jiang, X.; Zhang, L.; Quan, L. N.; Quintero-Bermudez, R.; Sutherland, B. R.; Mi, Q.; Sargent, E. H.; Ning, Z. Highly Oriented Low-Dimensional Tin Halide Perovskites with Enhanced Stability and Photovoltaic Performance. *J. Am. Chem. Soc.* **2017**, *139* (19), 6693−6699.
(14) Gong, X.; Voznyy, O.; Jain, A.; Liu, W.; Sabatini, R.; Piontkowski, Z.; Walters, G.; Bappi, G.; Nokhrin, S.; Bushuyev, O.; Yuan, M.; Comin, R.; McCamant, D.; Kelley, S. O.; Sargent, E. H. Electron−phonon interaction in efficient perovskite blue emitters. *Nat. Mater.* **2018**, *17* (6), 550−556.
(15) Liao, C.-H.; Mahmud, M. A.; Ho-Baillie, A. W. Y. Recent progress in layered metal halide perovskites for solar cells, photodetectors, and field-effect transistors. *Nanoscale* **2023**, *15* (9), 4219−4235.
(16) Gao, Y.; Wei, Z.; Yoo, P.; Shi, E.; Zeller, M.; Zhu, C.; Liao, P.; Dou, L. Highly Stable Lead-Free Perovskite Field-Effect Transistors Incorporating Linear π-Conjugated Organic Ligands. *J. Am. Chem. Soc.* **2019**, *141* (39), 15577−15585.
(17) Yang, W.; Dou, L.; Zhu, H.; Noh, Y.-Y. Ruddlesden−Popper Tin-Based Halide Perovskite Field-Effect Transistors. *Small Struct.* **2024**, *5*, 2300393.
(18) Worku, M.; Ben-Akacha, A.; Sridhar, S.; Frick, J. R.; Yin, S.; He, Q.; Robb, A. J.; Chaaban, M.; Liu, H.; Winfred, J. S. R. V.; Hanson, K.; So, F.; Dougherty, D.; Ma, B. Band Edge Control of Quasi-2D Metal Halide Perovskites for Blue Light-Emitting Diodes with Enhanced Performance. *Adv. Funct. Mater.* **2021**, *31* (45), 2103299.
(19) Ma, D.; Lin, K.; Dong, Y.; Choubisa, H.; Proppe, A. H.; Wu, D.; Wang, Y.-K.; Chen, B.; Li, P.; Fan, J. Z.; Yuan, F.; Johnston, A.; Liu, Y.; Kang, Y.; Lu, Z.-H.; Wei, Z.; Sargent, E. H. Distribution control enables efficient reduced-dimensional perovskite LEDs. *Nature* **2021**, *599* (7886), 594−598.
(20) Wang, H.-P.; Li, S.; Liu, X.; Shi, Z.; Fang, X.; He, J.-H. Low-Dimensional Metal Halide Perovskite Photodetectors. *Adv. Mater.* **2021**, *33* (7), 2003309.
(21) Wei, M.; Xiao, K.; Walters, G.; Lin, R.; Zhao, Y.; Saidaminov, M. I.; Todorović, P.; Johnston, A.; Huang, Z.; Chen, H.; Li, A.; Zhu, J.; Yang, Z.; Wang, Y.-K.; Proppe, A. H.; Kelley, S. O.; Hou, Y.; Voznyy, O.; Tan, H.; Sargent, E. H. Combining Efficiency and Stability in Mixed Tin−Lead Perovskite Solar Cells by Capping Grains with an Ultrathin 2D Layer. *Adv. Mater.* **2020**, *32* (12), 1907058.
(22) Tsai, H.; Nie, W.; Blancon, J.-C.; Stoumpos, C. C.; Asadpour, R.; Harutyunyan, B.; Neukirch, A. J.; Verduzco, R.; Crochet, J. J.; Tretiak, S.; Pedesseau, L.; Even, J.; Alam, M. A.; Gupta, G.; Lou, J.; Ajayan, P. M.; Bedzyk, M. J.; Kanatzidis, M. G.; Mohite, A. D. High-efficiency two-dimensional Ruddlesden−Popper perovskite solar cells. *Nature* **2016**, *536* (7616), 312−316.
(23) Park, S. M.; Mazza, S. M.; Liang, Z.; Abtahi, A.; Boehm, A. M.; Parkin, S. R.; Anthony, J. E.; Graham, K. R. Processing Dependent Influence of the Hole Transport Layer Ionization Energy on Methylammonium Lead Iodide Perovskite Photovoltaics. *ACS Appl. Mater. Interfaces* **2018**, *10* (18), 15548−15557.
(24) Liu, T.; Scheidt, R. A.; Zheng, X.; Joy, S.; Jiang, Q.; Atapattu, H. R.; Chen, M.; Pruett, H.; Zhu, K.; Luther, J. M.; Beard, M. C.; Graham, K. R. Tuning interfacial energetics with surface ligands to enhance perovskite solar cell performance. *Cell Rep. Phys. Sci.* **2023**, *4*, 101650.
(25) Shao, S.; Loi, M. A. The Role of the Interfaces in Perovskite Solar Cells. *Adv. Mater. Interfaces* **2020**, *7* (1), 1901469.
(26) Cao, D. H.; Stoumpos, C. C.; Yokoyama, T.; Logsdon, J. L.; Song, T.-B.; Farha, O. K.; Wasielewski, M. R.; Hupp, J. T.; Kanatzidis, M. G. Thin Films and Solar Cells Based on Semiconducting Two-Dimensional Ruddlesden−Popper $(CH_3(CH_2)_3NH_3)_2(CH_3NH_3)_{n-1}Sn_nI_{3n+1}$ Perovskites. *ACS Energy Lett.* **2017**, *2* (5), 982−990.
(27) Zhao, X.; Ball, M. L.; Kakekhani, A.; Liu, T.; Rappe, A. M.; Loo, Y.-L. A charge transfer framework that describes supramolecular interactions governing structure and properties of 2D perovskites. *Nat. Commun.* **2022**, *13* (1), 3970.
(28) Knutson, J. L.; Martin, J. D.; Mitzi, D. B. Tuning the Band Gap in Hybrid Tin Iodide Perovskite Semiconductors Using Structural Templating. *Inorg. Chem.* **2005**, *44* (13), 4699−4705.
(29) Du, K.-Z.; Tu, Q.; Zhang, X.; Han, Q.; Liu, J.; Zauscher, S.; Mitzi, D. B. Two-Dimensional Lead(II) Halide-Based Hybrid Perovskites Templated by Acene Alkylamines: Crystal Structures, Optical Properties, and Piezoelectricity. *Inorg. Chem.* **2017**, *56* (15), 9291−9302.
(30) Li, X.; Fu, Y.; Pedesseau, L.; Guo, P.; Cuthriell, S.; Hadar, I.; Even, J.; Katan, C.; Stoumpos, C. C.; Schaller, R. D.; Harel, E.; Kanatzidis, M. G. Negative Pressure Engineering with Large Cage Cations in 2D Halide Perovskites Causes Lattice Softening. *J. Am. Chem. Soc.* **2020**, *142* (26), 11486−11496.
(31) Ma, L.; Dai, J.; Zeng, X. C. Two-Dimensional Single-Layer Organic−Inorganic Hybrid Perovskite Semiconductors. *Adv. Energy Mater.* **2017**, *7* (7), 1601731.
(32) Kamminga, M. E.; Fang, H.-H.; Filip, M. R.; Giustino, F.; Baas, J.; Blake, G. R.; Loi, M. A.; Palstra, T. T. M. Confinement Effects in Low-Dimensional Lead Iodide Perovskite Hybrids. *Chem. Mater.* **2016**, *28* (13), 4554−4562.
(33) Mercier, N.; Poiroux, S.; Riou, A.; Batail, P. Unique Hydrogen Bonding Correlating with a Reduced Band Gap and Phase Transition in the Hybrid Perovskites (HO(CH2)2NH3)2PbX4 (X = I, Br). *Inorg. Chem.* **2004**, *43* (26), 8361−8366.
(34) Sourisseau, S.; Louvain, N.; Bi, W.; Mercier, N.; Rondeau, D.; Boucher, F.; Buzaré, J.-Y.; Legein, C. Reduced Band Gap Hybrid Perovskites Resulting from Combined Hydrogen and Halogen Bonding at the Organic−Inorganic Interface. *Chem. Mater.* **2007**, *19* (3), 600−607.

https://doi.org/10.1021/jacs.5c08621
J. Am. Chem. Soc. 2025, 147, 26898−26906

(35) Ashari-Astani, N.; Jahanbakhshi, F.; Mladenović, M.; Alanazi, A. Q. M.; Ahmadabadi, I.; Ejtehadi, M. R.; Dar, M. I.; Grätzel, M.; Rothlisberger, U. Ruddlesden−Popper Phases of Methylammonium-Based Two-Dimensional Perovskites with 5-Ammonium Valeric Acid AVA2MAn−1PbnI3n+1 with n = 1, 2, and 3. *J. Phys. Chem. Lett.* **2019**, *10* (13), 3543−3549.
(36) Zhong, X.; Ni, X.; Kaplan, A.; Zhao, X.; Ivancevic, M.; Ball, M. L.; Xu, Z.; Li, H.; Rand, B. P.; Loo, Y.-L.; Brédas, J.-L.; Kahn, A. Evolution of the Electronic and Excitonic Properties in 2D Ruddlesden−Popper Perovskites Induced by Bifunctional Ligands. *Adv. Energy Mater.* **2024**, *14* (18), 2304345.
(37) Silver, S.; Xun, S.; Li, H.; Brédas, J.-L.; Kahn, A. Structural and Electronic Impact of an Asymmetric Organic Ligand in Diammonium Lead Iodide Perovskites. *Adv. Energy Mater.* **2020**, *10* (14), 1903900.
(38) Zhong, X.; Ni, X.; Sidhik, S.; Li, H.; Mohite, A. D.; Brédas, J.-L.; Kahn, A. Direct Characterization of Type-I Band Alignment in 2D Ruddlesden−Popper Perovskites. *Adv. Energy Mater.* **2022**, *12* (45), 2202333.
(39) Qiu, L.; He, S.; Ono, L. K.; Qi, Y. Progress of Surface Science Studies on ABX3-Based Metal Halide Perovskite Solar Cells. *Adv. Energy Mater.* **2020**, *10* (13), 1902726.
(40) Endres, J.; Egger, D. A.; Kulbak, M.; Kerner, R. A.; Zhao, L.; Silver, S. H.; Hodes, G.; Rand, B. P.; Cahen, D.; Kronik, L.; Kahn, A. Valence and Conduction Band Densities of States of Metal Halide Perovskites: A Combined Experimental−Theoretical Study. *J. Phys. Chem. Lett.* **2016**, *7* (14), 2722−2729.
(41) Silver, S.; Yin, J.; Li, H.; Brédas, J.-L.; Kahn, A. Characterization of the Valence and Conduction Band Levels of n = 1 2D Perovskites: A Combined Experimental and Theoretical Investigation. *Adv. Energy Mater.* **2020**, *10* (46), 2000390.
(42) Shin, D.; Zu, F.; Nandayapa, E. R.; Frohloff, L.; Albert, E.; List-Kratochvil, E. J. W.; Koch, N. The Electronic Properties of a 2D Ruddlesden-Popper Perovskite and its Energy Level Alignment with a 3D Perovskite Enable Interfacial Energy Transfer. *Adv. Funct. Mater.* **2023**, *33* (2), 2208980.
(43) Lanzetta, L.; Marin-Beloqui, J. M.; Sanchez-Molina, I.; Ding, D.; Haque, S. A. Two-Dimensional Organic Tin Halide Perovskites with Tunable Visible Emission and Their Use in Light-Emitting Devices. *ACS Energy Lett.* **2017**, *2* (7), 1662−1668.
(44) Kashani, S.; Rech, J. J.; Liu, T.; Baustert, K.; Ghaffari, A.; Angunawela, I.; Xiong, Y.; Dinku, A.; You, W.; Graham, K.; Ade, H. Exciton Binding Energy in Organic Polymers: Experimental Considerations and Tuning Prospects. *Adv. Energy Mater.* **2024**, *14* (6), 2302837.
(45) Yoshida, H. Near-ultraviolet inverse photoemission spectroscopy using ultra-low energy electrons. *Chem. Phys. Lett.* **2012**, *539*−*540*, 180−185.
(46) Papavassiliou, G. C.; Koutselas, I. B.; Terzis, A.; Whangbo, M. H. Structural and electronic properties of the natural quantum-well system $(C_6H_5CH_2CH_2NH_3)_2SnI_4$. *Solid State Commun.* **1994**, *91* (9), 695−698.
(47) Hansen, K. R.; McClure, C. E.; Powell, D.; Hsieh, H.-C.; Flannery, L.; Garden, K.; Miller, E. J.; King, D. J.; Sainio, S.; Nordlund, D.; Colton, J. S.; Whittaker-Brooks, L. Low Exciton Binding Energies and Localized Exciton−Polaron States in 2D Tin Halide Perovskites. *Adv. Opt. Mater.* **2022**, *10* (9), 2102698.
(48) Ding, G.; He, X.; Zhang, H.; Fu, H. Ethanol-assisted synthesis of two-dimensional tin(ii) halide perovskite single crystals for amplified spontaneous emission. *J. Mater. Chem. C* **2022**, *10* (30), 10902−10907.
(49) Heimel, G.; Romaner, L.; Zojer, E.; Bredas, J.-L. The Interface Energetics of Self-Assembled Monolayers on Metals. *Acc. Chem. Res.* **2008**, *41* (6), 721−729.
(50) Heimel, G.; Salzmann, I.; Duhm, S.; Koch, N. Design of Organic Semiconductors from Molecular Electrostatics. *Chem. Mater.* **2011**, *23* (3), 359−377.
(51) Duhm, S.; Heimel, G.; Salzmann, I.; Glowatzki, H.; Johnson, R. L.; Vollmer, A.; Rabe, J. P.; Koch, N. Orientation-dependent ionization energies and interface dipoles in ordered molecular assemblies. *Nat. Mater.* **2008**, *7* (4), 326−332.
(52) Chen, W.; Qi, D. C.; Huang, Y. L.; Huang, H.; Wang, Y. Z.; Chen, S.; Gao, X. Y.; Wee, A. T. S. Molecular Orientation Dependent Energy Level Alignment at Organic−Organic Heterojunction Interfaces. *J. Phys. Chem. C* **2009**, *113* (29), 12832−12839.
(53) Schwarze, M.; Schellhammer, K. S.; Ortstein, K.; Benduhn, J.; Gaul, C.; Hinderhofer, A.; Perdigón Toro, L.; Scholz, R.; Kublitski, J.; Roland, S.; Lau, M.; Poelking, C.; Andrienko, D.; Cuniberti, G.; Schreiber, F.; Neher, D.; Vandewal, K.; Ortmann, F.; Leo, K. Impact of molecular quadrupole moments on the energy levels at organic heterojunctions. *Nat. Commun.* **2019**, *10* (1), 2466.
(54) Reo, Y.; Choi, T.; Go, J.-Y.; Jeon, S.; Lim, B.; Zhu, H.; Liu, A.; Noh, Y.-Y. Precursor Solution Aging: A Universal Strategy Modulating Crystallization of Two-Dimensional Tin Halide Perovskite Films. *ACS Energy Lett.* **2023**, *8* (7), 3088−3094.
(55) Hossain, T.; Atapattu, H. R.; Pruett, H.; Rahman, M. T.; Pedersen, K. R.; Huckaba, A. J.; Parkin, S. R.; Graham, K. R. Effects of A-Site Cation Structure on the Stability of 2D Tin Halide Perovskites. *Chem. Mater.* **2024**, *36* (22), 11004−11014.
(56) Shi, T.; Zhang, H.-S.; Meng, W.; Teng, Q.; Liu, M.; Yang, X.; Yan, Y.; Yip, H.-L.; Zhao, Y.-J. Effects of organic cations on the defect physics of tin halide perovskites. *J. Mater. Chem. A* **2017**, *5* (29), 15124−15129.
(57) Meggiolaro, D.; Ricciarelli, D.; Alasmari, A. A.; Alasmary, F. A. S.; De Angelis, F. Tin versus Lead Redox Chemistry Modulates Charge Trapping and Self-Doping in Tin/Lead Iodide Perovskites. *J. Phys. Chem. Lett.* **2020**, *11* (9), 3546−3556.

https://doi.org/10.1021/jacs.5c08621
J. Am. Chem. Soc. 2025, 147, 26898−26906